Ferroelectrically modulate the Fermi level of graphene oxide to enhance SERS response

Mingrui Shao, Chang Ji, Jibing Tan, Baoqiang Du, Xiaofei Zhao, Jing Yu, Baoyuan Man, Kaichen Xu, Chao Zhang and Zhen Li

---

Related articles

Generation of super-resolved optical needle and multifocal array using graphene oxide metalenses
Hongtao Wang, Chenglong Hao, Han Lin, Yongtian Wang, Tian Lan, Cheng-Wei Qiu, Baohua Jia
Opto-Electronic Advances   2021 **4**, 200031   doi: 10.29026/oea.2021.200031

Laser scribed graphene for supercapacitors
Zhengfen Wan, Xi Chen, Min Gu
Opto-Electronic Advances   2021 **4**, 200079   doi: 10.29026/oea.2021.200079

More related article in Opto-Electron Journals Group website

OEA | Opto-Electronic Advances

http://www.oejournal.org/oea

OE_Journal   @OptoElectronAdv

Ferroelectrically modulate the Fermi level of graphene oxide to enhance SERS response

Mingrui Shao[1], Chang Ji[1], Jibing Tan[1], Baoqiang Du[1], Xiaofei Zhao[1], Jing Yu[1], Baoyuan Man[1], Kaichen Xu[2]*, Chao Zhang[1]* and Zhen Li[1]*

Surface-enhanced Raman scattering (SERS) substrates based on chemical mechanism (CM) have received widespread attentions for the stable and repeatable signal output due to their excellent chemical stability, uniform molecular adsorption and controllable molecular orientation. However, it remains huge challenges to achieve the optimal SERS signal for diverse molecules with different band structures on the same substrate. Herein, we demonstrate a graphene oxide (GO) energy band regulation strategy through ferroelectric polarization to facilitate the charge transfer process for improving SERS activity. The Fermi level (E_f) of GO can be flexibly manipulated by adjusting the ferroelectric polarization direction or the temperature of the ferroelectric substrate. Experimentally, kelvin probe force microscopy (KPFM) is employed to quantitatively analyze the E_f of GO. Theoretically, the density functional theory calculations are also performed to verify the proposed modulation mechanism. Consequently, the SERS response of probe molecules with different band structures (R6G, CV, MB, PNTP) can be improved through polarization direction or temperature changes without the necessity to redesign the SERS substrate. This work provides a novel insight into the SERS substrate design based on CM and is expected to be applied to other two-dimensional materials.

Keywords: surface-enhanced Raman scattering (SERS); ferroelectric PMN-PT; graphene oxide (GO); photo-induced charge transfer (PICT)

Introduction

Surface-enhanced Raman spectroscopy (SERS) has become a powerful analytical tool due to its high sensitivity and non-invasive nature since its discovery in 1974[1–3]. Thus far, there are two main origins of SERS: electromagnetic mechanism (EM) and chemical mechanism (CM)[4,5]. EM is derived from the amplified electromagnetic field induced by localized surface plasmon resonance (LSPR) around noble metal nanoparticles triggered by incident light, thereby increasing the Raman scattering cross section of nearby molecules[6,7]. Although the Raman signal of the adsorbed molecules can be significantly enhanced depending on EM, the negative effects brought by noble metals cannot be ignored, such as steep price, poor biocompatibility and distortion of Raman signals caused by strong metal-molecule interactions[8,9]. On the other hand, CM is closely related to charge transfer (CT) between the substrate and molecules[10]. CT results in further separation of positive and negative charges, increasing the polarizability of molecules and thus heightening the Raman scattering cross section[11]. This means that the key to improving the CM effect is to

facilitate the interfacial CT process. In addition, CM-based two-dimensional (2D) materials for SERS offer some irreplaceable advantages over EM-based noble metals, such as low cost, high specificity, superior biocompatibility, excellent signal homogeneity and strong maneuverability[12−16].

If the energy gap between the substrates and probe molecules is tuned to align with the excitation laser energy, photo-induced charge transfer (PICT) will be effectively enhanced through the "borrowing effect" of the Herzberg-Teller coupling term, and consequently improving the SERS signal. To this end, various strategies, such as electric field regulation[17,18], chemical doping[19−22], and gas molecular adsorption or desorption[23], have been developed to improve CM enhancement by manipulating Fermi level (E_f) or valence band (VB) and conduction band (CB) of substrates to match the highest occupied molecule orbital (HOMO) and the lowest unoccupied molecule orbital (LUMO) of the analyte. Feng et al. designed a nitrogen-doped graphene substrate where the E_f of graphene can be shifted by controlling the nitrogen doping level, thus achieving modulation of the CT efficiency with certain organic fluorescent molecules[19]. Seo et al. optimized the complementary resonance effects between the substrate and probe molecule by varying the oxygen concentration in the ReO_xS_y thin film[20]. Liang et al. developed a two-dimensional (2D) borocarbonitride (BCN) SERS platform with adjustable CB level by changing the carbon atomic ratio for detection of specific molecular with appropriate band structure[21]. Zhou et al. developed a molecular adsorption strategy to regulate the CT efficiency between rGO and target molecules by controlling the adsorption or desorption of gas molecules on rGO surface[23]. However, an inevitable problem of these similar approaches is that the characteristic of a SERS substrate is fixed after preparation, and only the probe molecules with specific band structure are efficient in detection. In addition, these methods are cumbersome to operate, which is not conducive to the convenient collection of the SERS signals of multispecies molecules with different energy band structures. Currently, it is of great significance to provide a solution with convenient adjustment of substrate's electronic property to flexibly regulate the CT efficiency between the substrate and probe molecules with different band structures.

Lead magnesium niobate-lead titanate (PMN-PT) is a ferroelectric material in which the asymmetric distribution of positive and negative charges leads to the formation of electric dipoles[24,25]. At a certain temperature T ($T < T_c \sim 135$ °C), the self-polarized electric field generated by the stacking of electric dipoles induces an equal number of opposite charges on each side. In this case, holes or electrons are induced in a plane perpendicular to the direction of polarization, providing an excellent opportunity to modulate the electronic properties of the material adsorbed on PMN-PT surface[26]. As a two-dimensional material with convenient preparation and good biocompatibility, graphene and its derivatives (graphene oxide (GO) and reduced graphene oxide (rGO)) have attracted intense interest in the field of biosensors and photodetector[27−32]. Since the proposal of graphene-enhanced Raman spectroscopy (GERS) by Zhang et al. in 2010[33], a great deal of work is reported on studying the mechanism and application of GERS[34−36]. As we all know, graphene is an excellent candidate for studying CM enhancement owing to the fact that it does not support plasmonic excitation in the visible range[37]. Furthermore, the linear dispersion of graphene for electrons with the density of states disappearing at the Dirac point allows the injection of relatively small numbers of charge carriers to alter significantly its electronic properties[38,39].

In this work, we provide an innovative SERS substrate of graphene oxide coupled ferroelectric PMN-PT (PMN-PT@GO). The relationship between the doping level of GO and ferroelectric polarization was investigated and more quantitative information about the E_f of GO is characterized by employing a Kelvin probe force microscopy. We found that the E_f of GO could be well manipulated by the control of the direction and degree of ferroelectric polarization, and the effect on the chemical Raman enhancement of GO was studied. The SERS signal of rhodamine 6G (R6G) is further enhanced under stronger p-type doping, and consequently, the detection line is reduced from $10^{−7}$ to $10^{−8}$ M. In particular, the E_f could be changed actively by altering the temperature of the substrate owing to the variation of the ferroelectric polarization of PMN-PT. As a result, the detection line of R6G is again reduced to $10^{−9}$ M due to the stronger p-type doping triggered by the stronger ferroelectric polarization at low temperature. More importantly, the SERS signals of crystal violet (CV), methylene blue (MB) and p-nitrothiophenol (PNTP) molecules with different energy band structures from R6G are also successfully enhanced by selectively setting the temperature of substrate without the need of redesigning the substrate structure. The energy band regulation strategy proposed

in this paper not only provides a new way to deeply understand the CM enhancement effect, but also is expected to be extended to other 2D materials due to the feasibility of ferroelectric modulation of semiconductor energy levels[40−44].

Results and discussion

SERS performance and mechanism study

In order to determine the type of charge induced on the surface of PMN-PT, the short-circuit current was measured firstly by applying temperature fluctuations. As shown in Fig. S1(b), under forward connection, a positive current was received when the temperature rose from 20 to 100 °C (dT/dt = 2.5 °C/s), and a corresponding negative current was observed when the temperature drops from 100 to 20 °C (dT/dt = −2.5 °C/s). Notely, under reversed connection, the obtained current signals were switched in sign (Fig. S1(d)), which is evidence that the electric signals are coming from the pyroelectric effect of ferroelectric PMN-PT[45,46]. This is because the inherent spontaneous polarization (P_s) of PMN-PT leads to the existence of opposite free charges on the same electrode when it is forward and reversed connected to the measurement system, separately (Fig. S1(a) and S1(c))[47]. Therefore, the polarization direction inside PMN-PT can be determined according to the pyroelectric current direction (see Section 1 in Supplementary information for details).

Next, based on the above detailed analysis of the polarization, GO was spin coated on both surface (perpendicular to the direction of P_s) of PMN-PT to prepare PMN-PT@GO (P_s^+, the polarization direction points to GO film) and PMN-PT@GO (P_s^-, the polarization direction departs from GO film) substrates, respectively. In addition, Al_2O_3 without ferroelectric effect was also selected to synthesize Al_2O_3@GO as a control group using the same method. The probe molecule R6G was employed to further investigate their SERS properties. As shown in Fig. 1(a), PMN-PT@GO(P_s^-) exhibits the best SERS activity with an enhancement factor (EF) of $7.0×10^3$, followed by Al_2O_3@GO with an EF of $4.2×10^3$, while PMN-PT@GO (P_s^+) is the weakest with an EF of $3.8×10^3$ (Fig. S2), which may be caused by the doping effect of PMN-PT on GO. SERS spectra taken from five random points of PMN-PT@GO(P_s^-), Al_2O_3@GO and PMN-PT@GO (P_s^+) were collected to evaluate the uniformity of R6G on the three samples, respectively. The

three spectral gradients show nearly identical signal intensity on their respective samples (Fig. S3), indicating the uniform SERS effect of GO due to the flat two-dimensional surface and the homogeneous adsorption of R6G on GO. It has been reported that the frequency of the G band is shifted by changes in carrier concentration of graphene. N-type or p-type doping causes opposite shifts of the G band, due to stiffening or softening of phonons[48]. It is noteworthy that, compared to the Raman frequency (1587 cm^{-1}) of the G band in Al_2O_3@GO, the Raman frequencies of the G band in PMN-PT@GO (P_s^+) and PMN-PT@GO(P_s^-) are red-shifted and blue-shifted to 1584 and 1593 cm^{-1}, respectively (Fig. 1(b)), corresponding to an increase and decrease in carrier concentration of $\sim 2 × 10^{12}$ cm^{-2} and $\sim 4 × 10^{12}$ cm^{-2} [49]. This suggests that the ferroelectric effect of PMN-PT can indeed change the carrier concentration of adsorbed GO (Fig. 1(d–f)), leading to a shift in the corresponding GO Fermi level, thus further affecting the PICT process between the substrates and the probe molecule, as described below. In addition, when R6G is adsorbed on GO, the change of absorption peak (~230 cm^{-1}) also indicates experimentally that SERS enhancement is related to the CT interaction between them (Fig. 1(c))[50].

Subsequently, the further band structure analysis was carried out to more clearly illustrate the PICT process. For R6G molecule, the HOMO and LUMO levels are −5.7 and −3.4 eV, respectively, with an energy interval ($\Delta E_{h\text{-}l}$) of 2.3 eV[51]. Molecular resonance (μ_{mol}) occurs because $\Delta E_{h\text{-}l}$ almost perfectly matches the energy of 532 nm excited laser (2.33 eV). Kelvin probe force microscopy (KPFM) was used to determine the E_f of GO for each sample using the gold probe with the E_f of −5.10 eV as a reference (see Section 4 in Supplementary information for details)[52]. The contact potential differences (V_{CPD}) between Au tip and GO in Al_2O_3@GO, PMN-PT@GO (P_s^+) and PMN-PT@GO(P_s^-) are −155, −225 and +250 mV, respectively, as shown in Fig. 1(g–i). Therefore, the Fermi levels of GO in Al_2O_3@GO, PMN-PT@GO (P_s^+) and PMN-PT@GO (P_s^-) are −4.95, −4.85, and −5.41 eV (vs E_{vac}), respectively. According to the above results, the corresponding SERS enhancement mechanism is proposed. Owing to the fact that the transition energy ($\Delta E_{f\text{-}l}$ = 1.55 eV) from the E_f of GO in Al_2O_3@GO to the LUMO of R6G is mismatched with incident photon energy, the PICT process is obstructed and thus cannot provide a satisfactory SERS effect, as depicted in Fig. 1(j). Even weaker SERS signal appears on
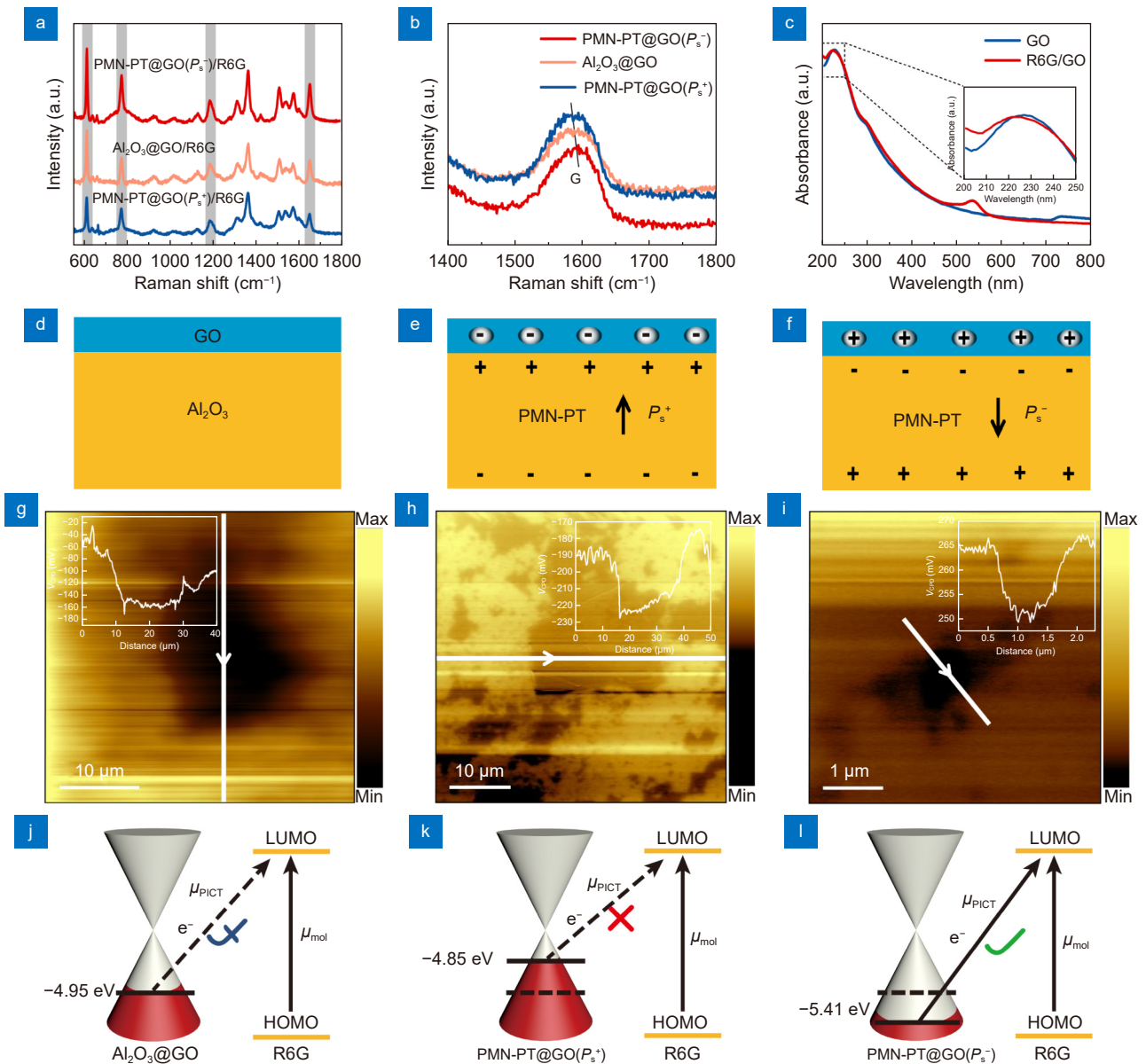
Fig. 1 | (a) SERS performance of Al_2O_3@GO, PMN-PT@GO (P_s^+) and PMN-PT@GO(P_s^-) by employing R6G as the probe molecule under excitation of 532 nm laser. **(b)** Raman shift of G band of GO in Al_2O_3@GO, PMN-PT@GO (P_s^+) and PMN-PT@GO(P_s^-). **(c)** UV-vis spectra of the GO and R6G/GO. **(d-f)** Schematic diagram of GO doping when adsorbed on different surfaces of PMN-PT. **(g-i)** Contact potential differences (V_{CPD}) between Au probe and GO in (g) Al_2O_3@GO, (h) PMN-PT@GO (P_s^+) and (i) PMN-PT@GO(P_s^-) measured by a KPFM system. **(j-l)** Modulation mechanism of SERS enhancement of **(j)** Al_2O_3@GO, **(k)** PMN-PT@GO (P_s^+) and **(l)** PMN-PT@GO(P_s^-).

PMN-PT@GO (P_s^+) due to further suppression of PICT by a narrower band gap ($\Delta E_{f\text{-}l}$ = 1.45 eV) than incident photon energy (Fig. 1(k)). However, the E_f of GO is closer to the HOMO of R6G due to the enhanced *p*-type doping of PMN-PT (P_s^-) on GO. The energy of PICT ($\Delta E_{f\text{-}l}$ = 2.01 eV) is better matched with incident photon energy, and consequently higher SERS activity is obtained (Fig. 1(l)). This phenomenon can also be easily understood by utilizing the polarization tensor formula: $\alpha_{\sigma\rho} = A + B + C$, where *A* represents molecular reson-

ance, which is associated with inter-band transitions within molecules, *B* refers to the surface plasmon resonance (SPR), and *C* denotes the PICT resonance at the Fermi level between substrate and molecule (see Section 5 in Supplementary information for details)[53]. Term *B* is not considered in this paper because the plasmonic excitation of graphene is powerfully confined to the range of terahertz/infrared spectral[54]. Among all samples, only PMN-PT@GO(P_s^-) can satisfy both the molecular resonance *A* and optimal PICT resonance *C*, where $\mu_{mol} \approx$

μ_{PICT}. In this case, the polarization tensor of molecular is significantly amplified through the Herzberg-Teller vibration coupling effect[55]. Therefore, PMN-PT@GO(P_s^-) exhibits the largest SERS activity. We also tested the enhancement properties of three samples against R6G molecules using a 785 nm laser (Fig. S5). Interestingly, only the Al_2O_3@GO exhibits characteristic peak of R6G due to the PICT resonance from the E_f of GO to the LUMO. However, the extremely weak signal compared to the obvious characteristic peaks under 532 nm laser excitation is due to the inability of 785 nm to trigger resonance Raman scattering (RRS or called molecular resonance).

To confirm the working mechanism, first-principles density functional theory (DFT) calculations were performed to study the interaction properties of graphene with ferroelectric PMN-PT polarization. Figure 2(a–c) show the constructed atomic structure model. The initial structure of PMN-PT was optimized with the polar-

ization direction normal to the graphene surface, including graphene on both the up-polarized (P_s^+) and down-polarized (P_s^-) surfaces. The opposite net surface charges appear on each side of the bulk ferroelectric PMN-PT owing to the polar stacking. These surface charges will be passivated by surface reconstruction, mobile charges, and in this case by graphene. In other words, graphene is responsible for providing additional compensation[49]. In intrinsic graphene, the Fermi level is located at the Dirac point energy (Fig. 2(d)). However, as a result of contact with the P_s^+ and P_s^- surfaces, the Dirac cone of graphene on the P_s^+ surface is shifted downward due to the increased electron density (Fig. 2(e)), and the Dirac cone of graphene on the P_s^- surface is shifted upward due to the decreased electron density (Fig. 2(f)), with respect to the Fermi level of intrinsic graphene. This indicates effective *n*-type or *p*-type doping in graphene. We emphasize that the simplified model is designed to capture the physical
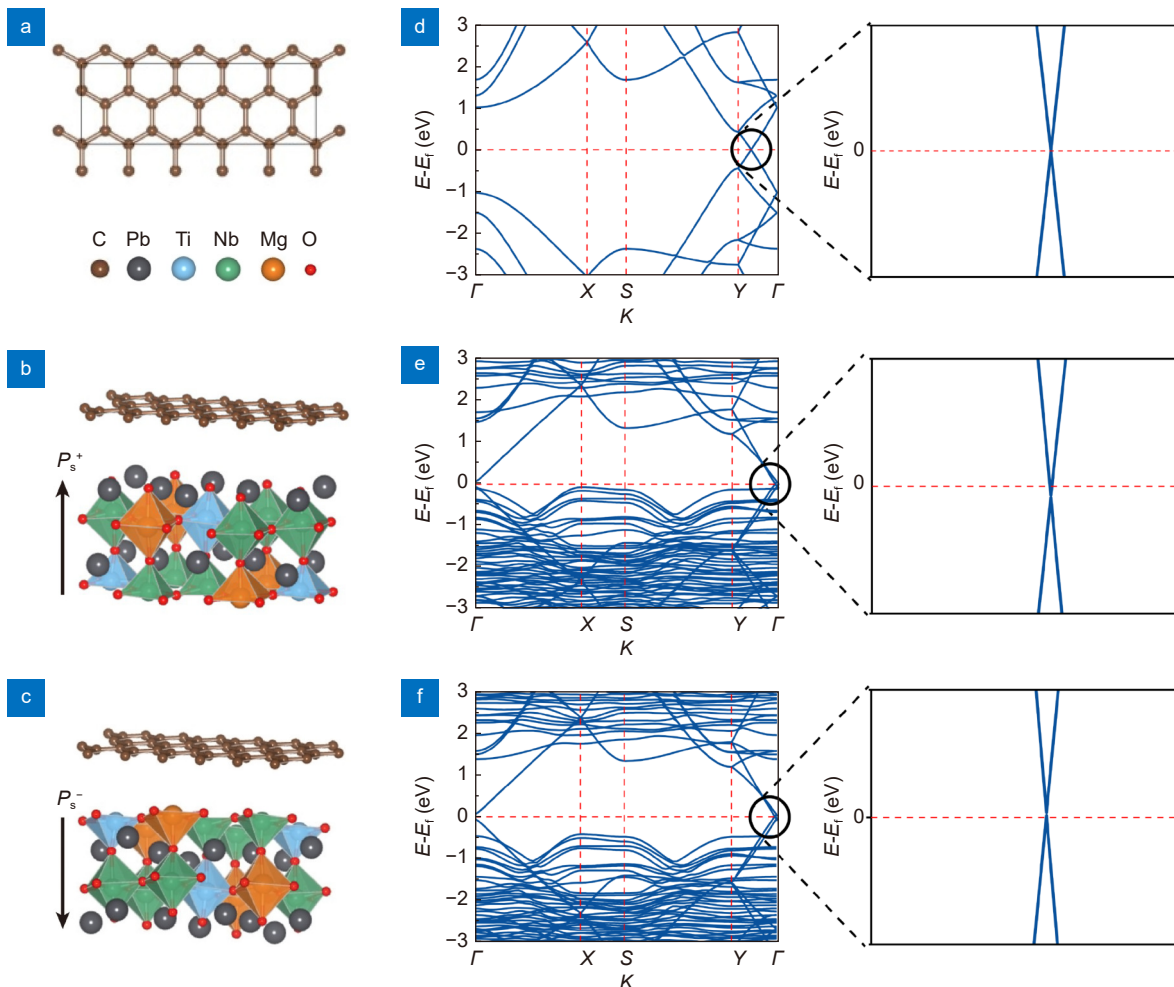

Fig. 2 | Atomic structure of (**a**) intrinsic graphene, (**b**) graphene on up-polarized (P_s^+) PMN-PT surface, (**c**) graphene on down-polarized (P_s^-) PMN-PT surface for DFT calculation. The electronic band structure of (**d**) intrinsic graphene, (**e**) graphene on up-polarized (P_s^+) PMN-PT surface, (**f**) graphene on down-polarized (P_s^-) PMN-PT surface.

nature of the problem, not to provide quantitative consistency with experiments. The theoretical results indeed prove that the self-polarized ferroelectric PMN-PT could realize the regulation of the Fermi level of graphene adsorbed on its surface, which in turn is responsible for the further enhancement of SERS signals of probe molecules.

Flexible regulation of PICT efficiency

It is well known that the polarization of ferroelectric materials varies with ambient temperature.[24,56] The variation of polarization affects the free charge density of the material surface[57]. Inspired, we carefully investigated the temperature-dependent SERS response behavior of PMN-PT@GO(P_s^-) due to the optimal SERS activity. As depicted in Fig. 3(a), the signal intensity of R6G decreases or increases as the temperature of PMN-PT@GO(P_s^-) rises or drops. This may be attributed to smaller or larger P_s^- inside PMN-PT caused by higher or lower temperature, and consequently changing the surface charge density (Fig. 3(b)). At room temperature,

PMN-PT possesses a certain strength of P_s^-, which will induce a certain number of holes in GO (Fig. 3(b-i) and 3(c-i)). At higher temperature, the smaller P_s^- inside PMN-PT induces fewer holes in GO, leading to the E_f to ascend, which attenuates the PICT effect (Fig. 3(b-ii) and 3(c-ii)). Contrarily, at lower temperature, the larger P_s^- inside PMN-PT induces more holes in GO, making the E_f fall and further closer to the HOMO of R6G (Fig. 3(b-iii) and 3(c-iii)). Notably, there is no significant change in SERS strength on Al$_2$O$_3$@GO, despite the presence of possible interfacial strain (Fig. 3(d)). To assess the sensitivity of PMN-PT@GO(P_s^-), the concentration gradient experiment was performed. As shown in Fig. 3(e), the detection limit of R6G is only 10^{-8} M at 20 °C due to the weak chemical enhancement compared to that of EM[58,59]. However, the characteristic peaks of R6G with the concentration of 10^{-9} M are still distinguished at 0 °C (Fig. 3(f) and Fig. S6). Differently, the Al$_2$O$_3$@GO substrate can only detect SERS signal of 10^{-7} M either at 0 °C or 20 °C (Fig. 3(g)). In a word, PMN-PT at lower temperature
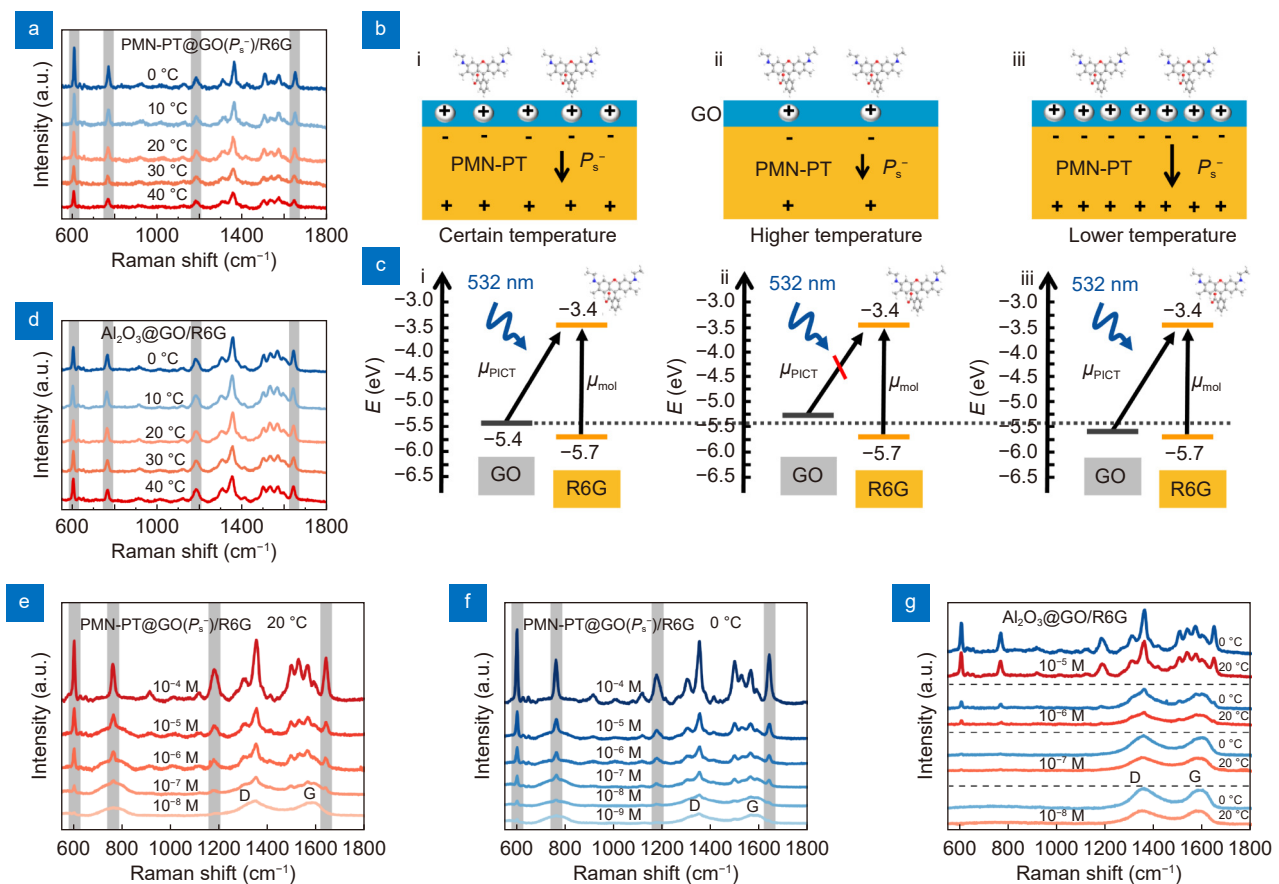
Fig. 3 | (a, d) The temperature-dependent SERS spectra of R6G by employing (a) PMN-PT@GO(P_s^-), (d) Al$_2$O$_3$@GO as a SERS substrate. **(b)** Schematic diagram of doping level of GO affected by PMN-PT@GO(P_s^-) temperature. **(c)** Schematic illustration of the energy band structure of PMN-PT@GO(P_s^-)/R6G and the electron transition process under 532 nm excitation laser. **(e, f)** SERS spectra of R6G with different concentrations on PMN-PT@GO(P_s^-) at (e) 20 °C, (f) 0 °C. **(g)** SERS spectra of R6G with different concentrations on Al$_2$O$_3$@GO at different temperature.

enables the E_f of GO better match with the HOMO of R6G, which significantly improves the SERS performance of PMN-PT@GO(P_s^-). In addition, temperature changes of substrate may trigger degradation of the molecule (Fig. S7). The SERS signal intensity did not decay significantly until after 150 cycles, which was not enough to affect the accuracy of the other temperature-related experiments results (within one or two cycles).

Influence of excited laser and analyte on SERS activity

A profoundly critical fact to note is that the CM effect strongly depends on the energy level arrangement of the substrate-molecule system and the wavelength of the excited laser. The different choices of excited laser and molecules to be tested greatly affect the CM enhancement factor of SERS substrate[60]. The SERS signal of R6G excited by 633 nm laser is much weaker than that excited by 532 nm laser (Fig. S8(a)). This is attributed to inactivated molecule resonance due to the insufficient energy of 633 nm laser (1.96 eV), indicating that molecule reson-

ance Raman scattering (RRS) plays a pivotal role in the total signal enhancement (Fig. 3(c-i) and Fig. S8(c-i))[61]. Interestingly, different from the case under 532 nm laser excitation, PMN-PT@GO(P_s^-) shows the strongest SERS activity at 20 °C under 633 nm laser excitation (Fig. S8(b)). That's because the energy required to jump from the E_f of GO to the LUMO of R6G at 20 °C already matches the energy of 633 nm laser. The upturn or downturn of the E_f would result in a mismatch of levels (Fig. S8(c-ii) and S8(c-iii)). In addition, CV was also employed to study the CM effect. As displayed in Fig. 4(a), the SERS signal of CV excited by 633 nm laser is stronger than that excited by 532 nm laser. For CV molecule, the HOMO and LUMO levels are −6.0 and −4.1 eV, respectively. Although the electron transition from HOMO to LUMO in CV can be activated by either 532 or 633 nm laser, the energy of 633 nm laser is better matched to the energy interval (1.9 eV) than that of 532 nm laser, as shown in Fig. 4(c-i) and 4(d-i). Thus, the molecule resonance of CV is enhanced with 633 nm laser excitation. Figure 4(e) and f show the temperature-dependent SERS
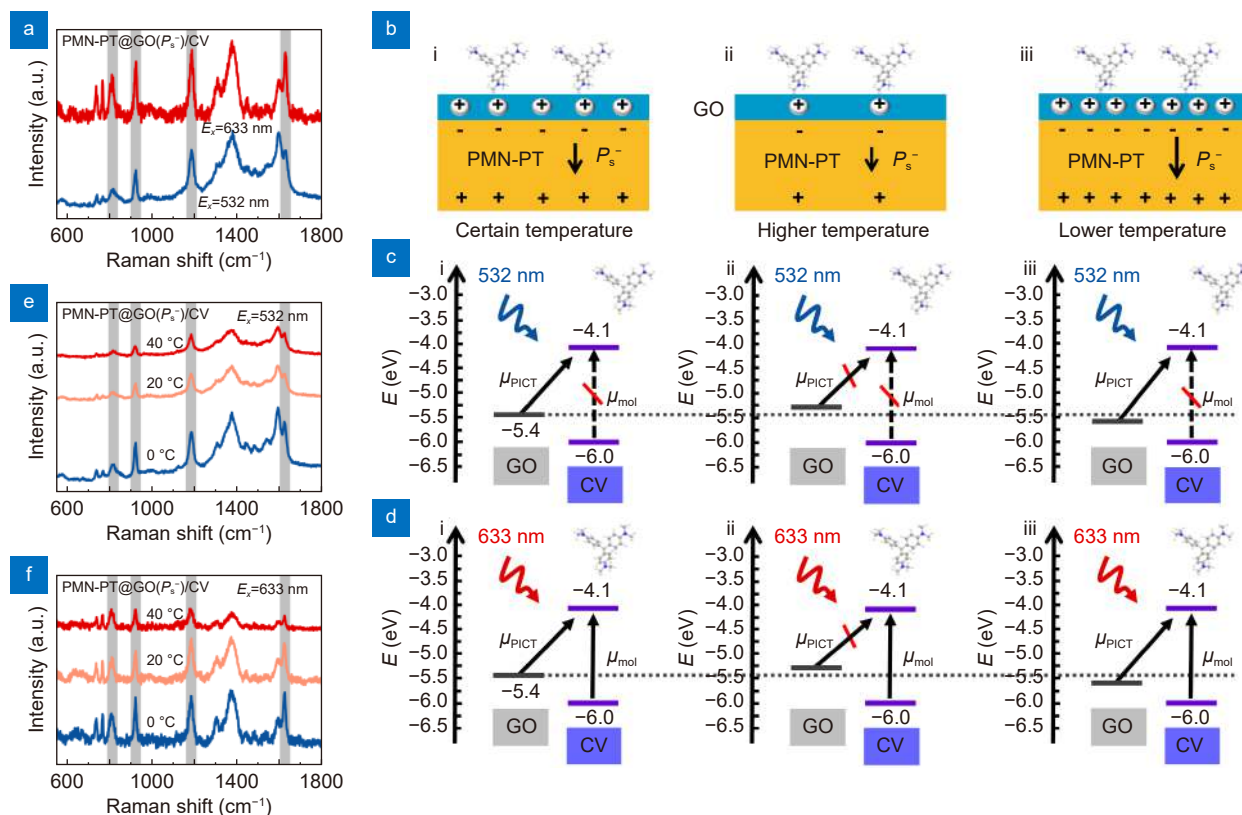
Fig. 4 | (**a**) SERS spectra of CV on PMN-PT@GO(P_s^-) under excitation of 532 and 633 nm laser. (**b**) Schematic diagram of doping level of GO affected by PMN-PT@GO(P_s^-) temperature. (**c**, **d**) Schematic illustration of the energy band structure of PMN-PT@GO(P_s^-)/CV and the electron transition process under (c) 532 nm, (d) 633 nm excitation laser. (**e**, **f**) SERS spectra of CV on PMN-PT@GO(P_s^-) under excitation of (e) 532 nm, (f) 633 nm laser at different temperature.

responses of CV molecule under excitation of 532 and 633 nm laser, respectively. Owing to the more effective PICT process, the strongest SERS signal is obtained at 0 °C in both cases (Fig. 4(c-iii) and 4(d-iii)). In synergy with the molecular resonance and the optimized PICT resonance, the detection limit of CV on PMN-PT@GO(P_s^-) substrate can also be optimized to 10^{-9} M (Fig. S9).

To further investigate the universality of the CM enhancement strategy proposed in this paper, MB and PNTP were also used to conduct SERS measurement. MB exhibits SERS modulation behavior similar to that of CV due to similar energy level structure (Fig. S10). However, since the large energy gap between the LUMO and HOMO in PNTP, molecule resonance cannot be activated with the insufficient excitation energy of either 532 or 633 nm laser (Fig. 5(d-i) and 5(e-i)). It is noteworthy that PNTP is better detected by PMN-PT@GO(P_s^-) at 40 °C, rather than at 0 °C with either 532 or 633 nm laser excitation (Fig. 5(a) and 5(b)), due to the more suitable energy position (Fig. 5(d-ii) and 5(e-ii)). For mixed solutions, as shown in Fig. S11, the SERS spectra of R6G and PNTP were selectively enhanced at 0 and 40 °C compared to that at 20 °C, respectively. There-

fore, the optimized SERS responses of molecules with different band structures can be obtained by flexibly adjusting the E_f of GO through simple temperature changes without the need to redesign the SERS substrate. Also, it should be pointed out that PMN-PT@GO (P_s^+) exhibits higher SERS activity than PMN-PT@GO(P_s^-) for PNTP (Fig. S12(a) and S12(b)). Higher E_f of PMN-PT@GO (P_s^+) is conducive for electrons in it to transition to the LUMO of PNTP (Fig. S12(c-ii) and S12(c-iv)). The corresponding temperature-dependent SERS spectra were also measured, and adjustable PICT efficiency was shown (Fig. S13). Although the PMN-PT@GO (P_s^+) substrate exhibited the highest SERS activity toward PNTP at 20 °C, its detection limit was only able to reach 10^{-7} M (Fig. S14), which may be due to the inactivated molecular resonance under 532 nm excitation laser (Fig. S13(d-i)).

Conclusions

In summary, we have presented a flexible energy band regulation strategy to manipulate the E_f of GO utilizing the ferroelectric PMN-PT for SERS detection of molecules with different band structures. The SERS signal is significantly enhanced after the energy gap between the E_f of GO and the LUMO of molecules is tuned to align
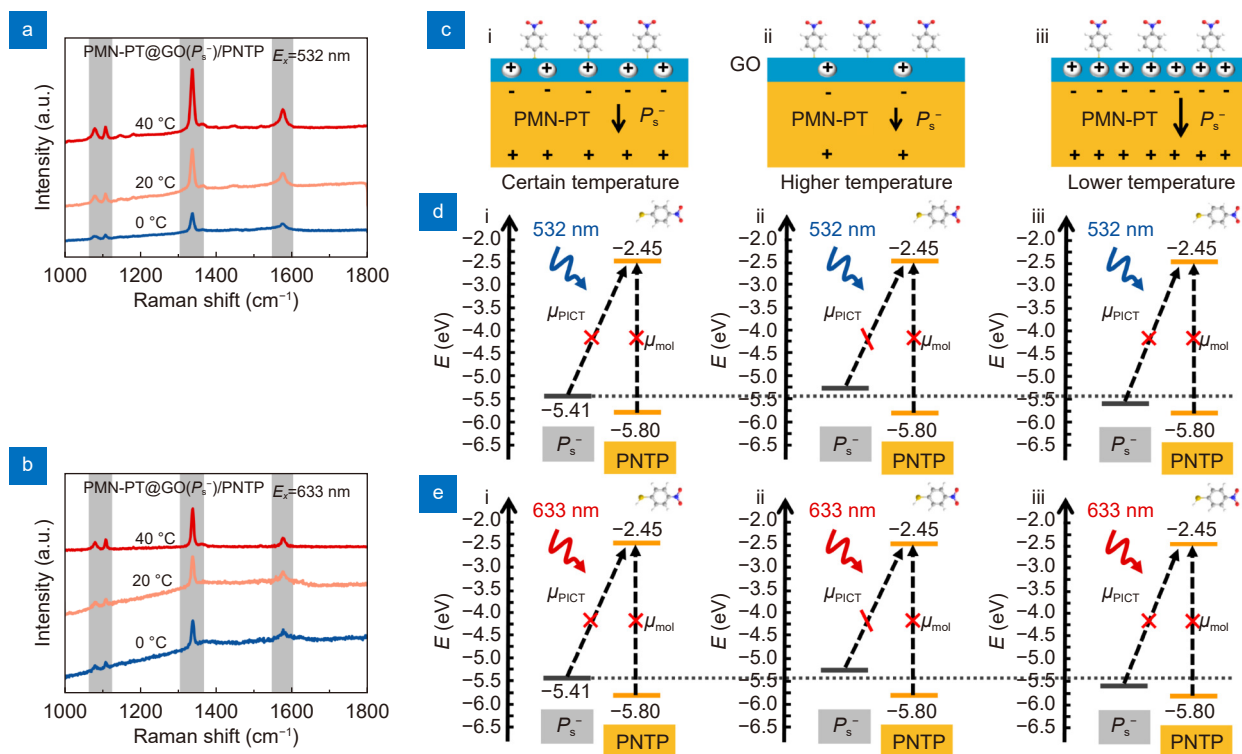
Fig. 5 | (**a**, **b**) SERS spectra of PNTP on PMN-PT@GO(P_s^-) under excitation of (a) 532 nm, (b) 633 nm laser at different temperature. (**c**) Schematic diagram of doping level of GO affected by PMN-PT@GO(P_s^-) temperature. (**d**, **e**) Schematic illustration of the energy band structure of PMN-PT@GO(P_s^-)/PNTP and the electron transition process under (d) 532 nm, (e) 633 nm excitation laser.

with the energy of excitation laser, due to the enhanced PICT efficiency. More importantly, this strategy provides new perspective for the SERS substrate design based on CM effect.

References

1. Wang X, Huang SC, Hu S, Yan S, Ren B. Fundamental understanding and applications of plasmon-enhanced Raman spectroscopy. *Nat Rev Phys* **2**, 253–271 (2020).

2. Chen XY, Ding QQ, Bi C, Ruan J, Yang SK. Lossless enrichment of trace analytes in levitating droplets for multiphase and multiplex detection. *Nat Commun* **13**, 7807 (2022).

3. Bharati MSS, Soma VR. Flexible SERS substrates for hazardous materials detection: recent advances. *Opto-Electron Adv* **4**, 210048 (2021).

4. Ding SY, Yi J, Li JF, Ren B, Wu DY et al. Nanostructure-based plasmon-enhanced Raman spectroscopy for surface analysis of materials. *Nat Rev Mater* **1**, 16021 (2016).

5. Du XJ, Liu D, An KY, Jiang SZ, Wei ZX et al. Advances in oxide semiconductors for surface enhanced Raman scattering. *Appl Mater Today* **29**, 101563 (2022).

6. Ding SY, You EM, Tian ZQ, Moskovits M. Electromagnetic theories of surface-enhanced Raman spectroscopy. *Chem Soc Rev* **46**, 4042–4076 (2017).

7. Zhao YY, Ren XL, Zheng ML, Jin F, Liu J et al. Plasmon-enhanced nanosoldering of silver nanoparticles for high-conductive nanowires electrodes. *Opto-Electron Adv* **4**, 200101 (2021).

8. Li SW, Miao P, Zhang YY, Wu J, Zhang B et al. Recent advances in plasmonic nanostructures for enhanced photocatalysis and electrocatalysis. *Adv Mater* **33**, 2000086 (2021).

9. Zhan C, Chen XJ, Huang YF, Wu DY, Tian ZQ. Plasmon-mediated chemical reactions on nanostructures unveiled by surface-enhanced raman spectroscopy. *Acc Chem Res* **52**, 2784–2792 (2019).

10. Kambhampati P, Child CM, Foster MC, Campion A. On the chemical mechanism of surface enhanced Raman scattering: Experiment and theory. *J Chem Phys* **108**, 5013–5026 (1998).

11. Zhang N, Tong LM, Zhang J. Graphene-based enhanced raman scattering toward analytical applications. *Chem Mater* **28**, 6426–6435 (2016).

12. Wang XT, Shi WX, Wang SX, Zhao HW, Lin J et al. Two-dimensional amorphous TiO_2 nanosheets enabling high-efficiency photoinduced charge transfer for excellent SERS activity. *J Am Chem Soc* **141**, 5856–5862 (2019).

13. Zheng ZH, Cong S, Gong WB, Xuan JN, Li GH et al. Semiconductor SERS enhancement enabled by oxygen incorporation. *Nat Commun* **8**, 1993 (2017).

14. Li MZ, Wei YJ, Fan XC, Li GQ, Hao Q et al. Mixed-dimensional van der Waals heterojunction-enhanced Raman scattering. *Nano Res* **15**, 637–643 (2022).

15. Peng YS, Lin CL, Long L, Masaki T, Tang M et al. Charge-transfer resonance and electromagnetic enhancement synergistically enabling MXenes with excellent SERS sensitivity for SARS-CoV-2 S protein detection. *Nano-Micro Lett* **13**, 52 (2021).

16. Tang X, Fan XC, Zhou J, Wang S, Li MZ et al. Alloy engineering allows on-demand design of ultrasensitive monolayer semiconductor SERS substrates. *Nano Lett* **23**, 7037–7045 (2023).

17. Xu H, Xie LM, Zhang HL, Zhang J. Effect of graphene fermi level on the raman scattering intensity of molecules on graphene. *ACS Nano* **5**, 5338–5344 (2011).

18. Xu H, Chen YB, Xu WG, Zhang HL, Kong J et al. Modulating the charge-transfer enhancement in GERS using an electrical field under vacuum and an n/p-doping atmosphere. *Small* **7**, 2945–2952 (2011).

19. Feng SM, dos Santos MC, Carvalho BR, Lv RT, Li Q et al. Ultrasensitive molecular sensor using N-doped graphene through enhanced Raman scattering. *Sci Adv* **2**, e1600322 (2016).

20. Seo J, Lee J, Kim Y, Koo D, Lee G et al. Ultrasensitive plasmon-free surface-enhanced raman spectroscopy with femtomolar detection limit from 2D van der waals heterostructure. *Nano Lett* **20**, 1620–1630 (2020).

21. Liang C, Lu ZA, Zheng M, Chen MX, Zhang YY et al. Band structure engineering within two-dimensional borocarbonitride nanosheets for surface-enhanced raman scattering. *Nano Lett* **22**, 6590–6598 (2022).

22. Li MZ, Wei YJ, Fan XC, Li GQ, Tang X et al. $VSe_{2-x}O_x$@Pd sensor for operando self-monitoring of palladium-catalyzed reactions. *JACS Au* **3**, 468–475 (2023).

23. Zhou L, Pusey-Nazzaro L, Ren GH, Chen LG, Liu LY et al. Photoactive control of surface-enhanced raman scattering with reduced graphene oxide in gas atmosphere. *ACS Nano* **16**, 577–587 (2022).

24. Fang HJ, Xu C, Ding J, Li Q, Sun JL et al. Self-powered ultrabroadband photodetector monolithically integrated on a PMN-PT ferroelectric single crystal. *Acs Appl Mater Interfaces* **8**, 32934–32939 (2016).

25. Pandya S, Wilbur J, Kim J, Gao R, Dasgupta A et al. Pyroelectric energy conversion with large energy and power density in relaxor ferroelectric thin films. *Nat Mater* **17**, 432–438 (2018).

26. Zheng R, Yan MY, Li C, Yin SQ, Chen WD et al. Pyroelectric effect mediated infrared photoresponse in Bi_2Te_3/Pb$(Mg_{1/3}Nb_{2/3})O_3$-$PbTiO_3$ optothermal ferroelectric field-effect transistors. *Nanoscale* **13**, 20657–20662 (2021).

27. Deng MH, Ren ZP, Zhang HB, Li ZQ, Xue CL et al. Unamplified and real-time label-free miRNA-21 detection using solution-gated graphene transistors in prostate cancer diagnosis. *Adv Sci* **10**, 2205886 (2023).

28. Romagnoli A, D'Agostino M, Pavoni E, Ardiccioni C, Motta S et al. SARS-CoV-2 multi-variant rapid detector based on graphene transistor functionalized with an engineered dimeric ACE2 receptor. *Nano Today* **48**, 101729 (2023).

29. Zhao L, Rosati G, Piper A, de Carvalho Castro e Silva C, Hu L et al. Laser reduced graphene oxide electrode for pathogenic escherichia coli detection. *ACS Appl Mater Interfaces* **15**, 9024–9033 (2023).

30. Guan HY, Hong JY, Wang XL, Ming JY, Zhang ZL et al. Broadband, high-sensitivity graphene photodetector based on ferroelectric polarization of lithium niobate. *Adv Opt Mater* **9**, 2100245 (2021).

31. Gopalan KK, Janner D, Nanot S, Parret R, Lundeberg MB et al. Mid-infrared pyroresistive graphene detector on $LiNbO_3$. *Adv Opt Mater* **5**, 1600723 (2017).

32. Lu YY, Yang G, Shen YJ, Yang HY, Xu KC. Multifunctional flexible humidity sensor systems towards noncontact wearable electronics. *Nano-Micro Lett* **14**, 150 (2022).

33. Ling X, Xie LM, Fang Y, Xu H, Zhang HL et al. Can graphene be used as a substrate for raman enhancement? *Nano Lett* **10**, 553–561 (2010).

34. Li Z, Jiang SZ, Huo YY, Ning TY, Liu AH et al. 3D silver nanoparticles with multilayer graphene oxide as a spacer for surface enhanced Raman spectroscopy analysis. *Nanoscale* **10**, 5897–5905 (2018).

35. Almohammed S, Zhang FY, Rodriguez BJ, Rice JH. Electric field-induced chemical surface-enhanced raman spectroscopy enhancement from aligned peptide nanotube-graphene oxide templates for universal trace detection of biomolecules. *J Phys Chem Lett* **10**, 1878–1887 (2019).

36. Zhou TY, Xu C, Ren WC. Grain-boundary-induced ultrasensitive molecular detection of graphene film. *Nano Lett* **22**, 9380–9388 (2022).

37. Hao QZ, Morton SM, Wang B, Zhao YH, Jensen L et al. Tuning surface-enhanced Raman scattering from graphene substrates using the electric field effect and chemical doping. *Appl Phys Lett* **102**, 011102 (2013).

38. Neto AHC, Guinea F, Peres NMR, Novoselov KS, Geim AK. The electronic properties of graphene. *Rev Mod Phys* **81**, 109–162 (2009).

39. Gorecki J, Apostolopoulos V, Ou JY, Mailis S, Papasimakis N. Optical gating of graphene on photoconductive Fe: $LiNbO_3$. *ACS Nano* **12**, 5940–5945 (2018).

40. Sun XZ, Chen Y, Zhao DY, Taniguchi T, Watanabe K et al. Measuring band modulation of MoS_2 with ferroelectric gates. *Nano Lett* **23**, 2114–2120 (2023).

41. Wang XD, Wang P, Wang JL, Hu WD, Zhou XH et al. Ultrasensitive and broadband MoS_2 photodetector driven by ferroelectrics. *Adv Mater* **27**, 6575–6581 (2015).

42. Zhang SK, Jiao HX, Wang XD, Chen Y, Wang HL et al. Highly sensitive InSb nanosheets infrared photodetector passivated by ferroelectric polymer. *Adv Funct Mater* **30**, 2006156 (2020).

43. Yan JM, Ying JS, Yan MY, Wang ZC, Li SS et al. Optoelectronic coincidence detection with two-dimensional Bi_2O_2Se ferroelectric field-effect transistors. *Adv Funct Mater* **31**, 2103982 (2021).

44. Chen JW, Lo ST, Ho SC, Wong SS, Vu THY et al. A gate-free monolayer WSe_2 pn diode. *Nat Commun* **9**, 3143 (2018).

45. Yang Y, Guo WX, Pradel KC, Zhu G, Zhou YS et al. Pyroelectric nanogenerators for harvesting thermoelectric energy. *Nano Lett* **12**, 2833–2838 (2012).

46. Ma N, Zhang KW, Yang Y. Photovoltaic-pyroelectric coupled effect induced electricity for self-powered photodetector system. *Adv Mater* **29**, 1703694 (2017).

47. Ma N, Yang Y. Enhanced self-powered UV photoresponse of ferroelectric $BaTiO_3$ materials by pyroelectric effect. *Nano Energy* **40**, 352–359 (2017).

48. Das B, Voggu R, Rout CS, Rao CNR. Changes in the electronic structure and properties of graphene induced by molecular charge-transfer. *Chem Commun* 5155–5157 (2008).

49. Baeumer C, Saldana-Greco D, Martirez JMP, Rappe AM, Shim M et al. Ferroelectrically driven spatial carrier density modulation in graphene. *Nat Commun* **6**, 6136 (2015).

50. Liu DM, Yi WC, Fu YL, Kong QH, Xi GC. In situ surface restraint-induced synthesis of transition-metal nitride ultrathin nanocrystals as ultrasensitive sers substrate with ultrahigh durability. *ACS Nano* **16**, 13123–13133 (2022).

51. Ge YC, Wang F, Yang Y, Xu Y, Ye Y et al. Atomically thin $TaSe_2$ film as a high-performance substrate for surface-enhanced raman scattering. *Small* **18**, 2107027 (2022).

52. Liu Y, Guo J, Zhu EB, Liao L, Lee SJ et al. Approaching the Schottky-Mott limit in van der Waals metal-semiconductor junctions. *Nature* **557**, 696–700 (2018).

53. Lombardi JR, Birke RL. A unified approach to surface-enhanced Raman spectroscopy. *J Phys Chem C* **112**, 5605–5617 (2008).

54. Jablan M, Buljan H, Soljačić M. Plasmonics in graphene at infrared frequencies. *Phys Rev B* **80**, 245435 (2009).

55. Lombardi JR, Birke RL. The theory of surface-enhanced Raman scattering. *J Chem Phys* **136**, 144704 (2012).

56. Li HY, Bowen CR, Yang Y. Phase transition enhanced pyroelectric nanogenerators for self-powered temperature sensors. *Nano Energy* **102**, 107657 (2022).

57. Yang Y, Wang SH, Zhang Y, Wang ZL. Pyroelectric nanogenerators for driving wireless sensors. *Nano Lett* **12**, 6408–6413 (2012).

58. Bai S, Serien D, Hu AM, Sugioka K. 3D microfluidic surface-enhanced raman spectroscopy (SERS) chips fabricated by all-femtosecond-laser-processing for real-time sensing of toxic substances. *Adv Funct Mater* **28**, 1706262 (2018).

59. Wu J, Du YJ, Wang CY, Bai S, Zhang T et al. Reusable and long-life 3D Ag nanoparticles coated Si nanowire array as sensitive SERS substrate. *Appl Surf Sci* **494**, 583–590 (2019).

60. Chen MM, Liu ZH, Su BH, Hu RJ, Fu FF et al. High-performance hydrogel SERS chips with tunable localized surface plasmon resonance for coordinated electromagnetic enhancement with chemical enhancement. *Adv Opt Mater* **11**, 2202852 (2023).

61. Cong S, Liu XH, Jiang YX, Zhang W, Zhao ZG. Surface enhanced raman scattering revealed by interfacial charge-transfer transitions. *Innovation* **1**, 100051 (2020).

Acknowledgements

Author contributions

M. R. Shao proposed and implemented experiments, analyzed data, and wrote and revised the manuscript. C. Ji, J. B. Tan, B. Q. Du, X. F. Zhao, J. Yu and B. Y. Man reviewed and revised the manuscript. K. C. Xu, C. Zhang, and Z. Li proposed and supervised the project and revised and determined the manuscript. All authors contributed to interpretation of the results and approved the submitted version.

Competing interests

Supplementary information

Supplementary information for this paper is available at
https://doi.org/10.29026/oea.2023.230094